Computers and Concrete, *Vol. 26, No. 3* (*2020*) *257-273*
DOI: https://doi.org/10.12989/cac.2020.26.3.257

Bonding of nano-modified concrete with steel under freezing temperatures using different protection methods

A.M. Yasien[1a] and M.T. Bassuoni*[2]

[1]*Civil Engineering, University of Manitoba, Winnipeg, Canada; Assistant Researcher, National Research Centre, Cairo, Egypt*
[2]*Civil Engineering, University of Manitoba, Winnipeg, Canada*

(*Received July 27, 2020, Revised August 24, 2020, Accepted September 3, 2020*)

Abstract. Concrete bond strength with steel re-bars depends on multiple factors including concrete-steel interface and mechanical properties of concrete. However, the hydration development of cementitious paste, and in turn the mechanical properties of concrete, are negatively affected by cold weather. This study aimed at exploring the concrete-steel bonding behavior in concrete cast and cured under freezing temperatures. Three concrete mixtures were cast and cured at -10 and -20°C. The mixtures were protected using conventional insulation blankets and a hybrid system consisting of insulation blankets and phase change materials. The mixtures comprised General Use cement, fly ash (20%), nano-silica (6%) and calcium nitrate-nitrite as a cold weather admixture system. The mixtures were tested in terms of internal temperature, compressive, tensile strengths, and modulus of elasticity. In addition, the bond strength between concrete and steel re-bars were evaluated by a pull-out test, while the quality of the interface between concrete and steel was assessed by thermal and microscopy studies. In addition, the internal heat evolution and force-slip relationship were modeled based on energy conservation and stress-strain relationships, respectively using three-dimensional (3D) finite-element software. The results showed the reliability of the proposed models to accurately predict concrete heat evolution as well as bond strength relative to experimental data. The hybrid protection system and nano-modified concrete mixtures produced good quality concrete-steel interface with adequate bond strength, without need for heating operations before casting and during curing under freezing temperatures down to -20°C.

Keywords: nano-silica; phase change materials; freezing; bonding; modeling

1. Introduction

The capacity of reinforced concrete elements is affected by the concrete-steel bonding, which defines their structural and ductility performance (MacGregor *et al.* 1997). However, concrete placement and curing under cold weather negatively affect its hydration development, mechanical properties, and consequently the concrete-steel bond strength (Neville 2011, Rixom and Mailvaganam 2002). Guidelines and codes for concrete (e.g., ACI 306R 2016, CSA A23.1 2019, CS164 2016) set 4 to 5°C as the benchmark for cold weather precautions. When the ambient temperature reaches these values, hydration of cementitious binders proceeds at very slow rates and ceases when the temperature drops to -2.8°C due to freezing of mixing water (Karagöl *et al.* 2015, Ratinov and Rozenberg 1996, Korhonen *et al.* 1992). Concrete produced under such conditions suffers from heterogonous microstructure and cracked matrix, which negatively affects its structural performance and service life (Prado *et al.* 1998, Powers and Helmuth 1953).

The aforementioned codes/guides ACI 306R (2016), CSA A23.1 (2019) have stipulations for cold weather concreting, including limitations on mixing, placement and curing temperatures, which can be achieved by heating concrete constituents (aggregates and water) between 40°C to 60°C, and building voluminous and heated enclosures to maintain concrete temperature at an acceptable threshold (more than 10°C) during placement and protection periods. In addition, ACI 306R (2016) recommends to heat any metallic embedments to at least 0°C when the ambient temperature is at or below -12°C to avoid ice formation at the interface and ensure adequate development in bond strength with concrete. However, such heating practices incur considerable costs due to massive energy consumption, required coverings/skilled labour and increased carbon footprint of construction (Barna *et al.* 2011). Consequently, in cold regions, the construction season is limited to warmer periods (from May to September in North America), leading to significant socioeconomic losses due to busy construction and backlogged repair schedules. Therefore, extending the construction season in cold regions is a critical issue, which necessitates continual advent of innovative strategies to cast and protect concrete efficiently under freezing temperatures.

In cold weather applications, the bonding between concrete and steel maybe inferior, because of the development of inadequately hydrated interfacial zone (Schroeder and Wood 1996). For instance, Schroeder and Wood (1996) investigated the effect of using calcium nitrite and sodium nitrite (cold weather admixture system; CWAS)

*Corresponding author, Professor
E-mail: mohamed.bassuoni@umanitoba.ca
[a]Ph.D. Candidate

ISSN: 1598-8198 (Print), 1598-818X (Online)

at dosages of 2% and 6% by mass of cement, respectively on concrete (cement content of 370 kg/m^3 and water-to-cement ratio of 0.48) bond strength with 20 mm steel bars. After casting specimen, using hot water (54°C) and room temperature steel bars, they were cured at average temperatures of -5 and -10°C. The bond strength of the specimens after 15 days of curing was less than 1 MPa and increased to 5.5 MPa after 28 days, which was markedly lower than that of similar concrete cured at normal temperatures (8 to 17 MPa) (Bahekar and Gadve 2019, Diab *et al.* 2014).

Since the last decade, the effects of vigorously reactive nanoparticles (e.g., nano-silica) on improving the hydration and microstructural development of concrete and its hardened properties have been the subject of extensive investigations (Ghazy *et al.* 2016, Mahdikhani and Ramezanianpour 2014, Madani *et al.* 2012). However, most of these studies were conducted for concrete produced and cured under normal temperatures (20 to 30°C), while research on the use of nanoparticles in cold weather concrete applications is still in early stages. For example, in recent studies by the authors (Yasien *et al*. 2019, Abayou *et al*. 2019), statistical modelling associated with experimental work were performed to develop winter concrete, using combinations of various water-to-binder ratios (*w/b*), fly ash, nano-silica and different antifreeze/accelerating CWAS, which was cast and cured under low temperatures down to -5°C without any heating or protection. It was found that low *w/b* (0.32) concrete mixtures incorporating 2 to 6% nano-silica and calcium nitrate-nitrite solutions (CNAI), without and with fly ash, achieved acceptable performance in terms of hardening rates, hydration development, strength and durability properties (Yasien *et al*. 2019, Abayou *et al*. 2019). However, the bonding behaviour of these mixtures with unheated metallic reinforcement at freezing temperatures has not been investigated, which warrants further studies in this direction.

On the other hand, incorporating phase change materials (PCM), energy absorbing/release reservoirs that can reversibly store and emit heat through solidifying/melting processes (Aguayo *et al*. 2016, Fernandes *et al.* 2014), in concrete is a relatively new technique capable of enhancing concrete's thermal energy storage capacity. PCM can be integrated into concrete matrices by direct incorporation during mixing (Liu *et al.* 2017, Fernandes *et al.* 2014), micro (Liu *et al.* 2017), or macro-encapsulation (Farnam *et al*. 2015) as well as saturation of lightweight aggregates (Farnam *et al*. 2015), or nano-materials such as nano-silica (Li *et al.* 2015), and carbon nanotubes (Dorigato *et al.* 2017). Among all types of PCM, organic PCM, paraffin or non-paraffin, are preferred to be used in concrete applications due to their noncorrosive and stable nature as well as operating temperatures (Baetens *et al.* 2010). These materials have been commonly utilized to improve the resistance of concrete to freezing-thawing cycles by delaying ice formation (Meshgin and Xi 2012), and mitigating thermal cracking (Kim *et al.* 2015). However, the incorporation of PCM in concrete has its own drawbacks; it has marked negative effects on concrete mechanical and physical properties [reduction of strength/elastic modulus (Farnam *et al*. 2015), and high porosity (Aguayo *et al*. 2016) and drying shrinkage (Meshgin and Xi 2012), which may limit the applications of PCM-modified concrete to non-structural applications (Cao *et al.* 2017, Memon *et al.* 2015). Despite the potential of PCM to retain concrete internal temperature and delay ice formation between concrete and unheated metallic embedment and/or forms through its heat of fusion, the viability of using PCM as external curing aids in order to protect newly poured concrete under freezing temperatures has not been explored.

1.1 Research significance

Nano-modified concrete incorporating CWAS and protected using PCM as an external curing agent may offer a sustainable and cost-efficient option for cold weather concreting applications, without the need for extensive heating practices. Yet, this needs to be systematically investigated, which was the motive for this research. In comparison to a conventional protection method (insulation blankets), this study aimed at exploring the efficacy of using a hybrid protection system (insulation blanket + PCM mat) on hydration development and bonding behavior with steel of nano-modified concrete cured under freezing temperatures (-10 and -20°C), without heating. The experimental work included internal temperature, mechanical properties, bonding, thermal, and microstructural studies to evaluate the hydration development of the cementitious matrix at the concrete-steel interface. In addition, thermal and mechanical finite-element models were developed to numerically capture temperature stratification in concrete and resulting bonding strength with steel. The success of such protection methods and mixtures designs may provide an integrated strategy for alleviating heating requirements and improving the quality of winter concrete production in cold regions.

2. Experimental procedure

2.1 Materials and mixtures

General use (GU) cement and Class F fly ash, complying with CAN/CSA-A3001 (2018), were used as the main constituents of binders. A commercially available nano-silica sol (aqueous solution with 50% solid content of fully dispersed SiO_2) was added to produce nano-modified concrete in different mixtures as a partial replacement of cement. The mean particle size, specific gravity, and surface area of the nano-silica are 35 nm, 1.4 and 80,000 m^2/kg, respectively. The dosages of nano-silica and fly ash were fixed at 6% and 20%, respectively. For all mixtures, the total binder content and water-to-binder ratio (*w/b)* were kept constant at 400 kg/m^3 and 0.32, respectively. These proportions produced concrete with balanced performance in terms of fresh, hardened and durability when cast and cured under normal and low temperatures (23 to -5°C) (Yasien *et al*. 2019, Abayou *et al*. 2019, Ghazy *et al*. 2016). Well-graded river sand with fineness modulus of 2.9 and natural gravel with maximum size of 9.5 mm were used

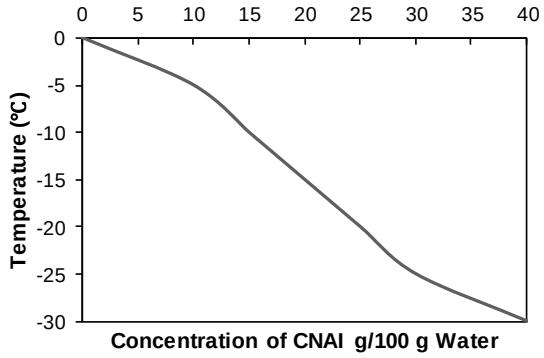

Fig. 1 Phase diagram of calcium nitrate-nitrite with ratio of 1:1 by mass

in this study. The specific gravity and absorption were 2.65 and 2%, respectively for gravel, and 2.53% and 1.5%, respectively for sand. A polycarboxylic acid-based high-range water reducing admixture (HRWRA), complying with ASTM C494 (2019), Type F was added to achieve a target consistency of 175±25 mm. An air entraining (AE) admixture, complying with ASTM C260/C260M (2016), was added to the different mixtures to achieve a target fresh air content of 6±1%.

A combination (CNAI) of calcium nitrate and calcium nitrite (antifreeze and accelerating admixtures) with a ratio of 1:1 by mass was used as CWAS, at a constant dosage of 15% by mass of the mixing water. According to the phase diagram of the combination (Fig. 1), this concentration was selected to depress the freezing point of mixing water down to -10°C to avoid freezing of mixing water during the first 2 to 4 hours, to allow for mixing, transporting and placement operations before applying any protection (refer to the Procedures Section). The proportions of the three mixtures tested are shown in Table 1. These mixtures were cast and cured at two freezing temperatures and protected by different methods. In the mixture ID, the letters GU, F, N denote GU cement, fly ash and nano-silica, respectively.

2.2 Procedures

Based on previous studies by the authors (Yasien *et al*. 2019, Abayou *et al*. 2019), mixing procedures were conducted at -5ºC inside an environmental chamber, where solid constituents of concrete were stored for 24 h prior to mixing. Conditioned cold mixing water (5±1ºC) was used to mimic realistic winter tap water condition. These temperatures simulate minimal heat conditioning for mixing concrete ingredients during winter. To ensure homogenous

Table 1 Mixtures proportions per cubic meter

Mixture ID.	Cement (kg)	Fly ash (kg)	Nano-silica (kg)	Water* (kg)	CNA†/CNI* (kg)	Coarse aggregate (kg)	Fine aggregate (kg)
GU	400	-	-	105.6	14+32	1156	622
GUN	376	-	48	81.6	14+32	1151	620
GUFN	296	80	48	81.6	14+32	1137	612

*Adjusted amount of water considering the water content of nano-silica (aqueous solution with 50% solid content of SiO_2) and CNI (aqueous solution with 30% solid content).
†The CNA admixture was in solid form with 70% active ingredient.

dispersion of mixtures' constituents, a particular sequence of mixing, which was developed earlier by the authors (Yasien *et al*. 2019, Abayou *et al*. 2019) based on trial batches, was followed. After mixing, concrete mixtures were cast in molds, with initial temperature similar to the curing temperatures, and kept inside another environmental chamber at two winter curing scenarios (-10 and -20ºC) till testing, using one of the adopted protection methods described below. To simulate wind conditions, the chambers were equipped with a fan to circulate air at an average speed of 25 km/h. Such freezing temperatures were selected to cover the common and practical range of winter temperatures for construction in many regions in North America and Europe.

2.3 Protection methods

Two different methods of protection, conventional and hybrid, were adopted during curing under freezing temperatures. For the conventional method, insulation blankets (designated as 'I') were used to cover the specimens. They were selected based on the *R-value* (capacity of an insulating material to resist heat flow; higher numbers designate greater efficiency) as recommended in ACI-306R (2016) Table 9.3a to protect ordinary concrete for 7 days in sections ≤200 mm (range of specimens' thicknesses). However, a reduction factor of 25% was applied to the *R-values* considering the satisfactory performance of the adopted mixtures under -5°C without protection (Yasien *et al*. 2019, Abayou *et al*. 2019); thus, the *R-values* of the insulation blankets were 5 and 7 for -10 and -20°C curing temperatures, respectively.

Moreover, the efficacy of applying paraffin-based PCM as a renewable and sustainable curing aid for the mixtures was explored. A reusable PCM mat was attached to the insulation blanket without/with a reflective layer as a hybrid

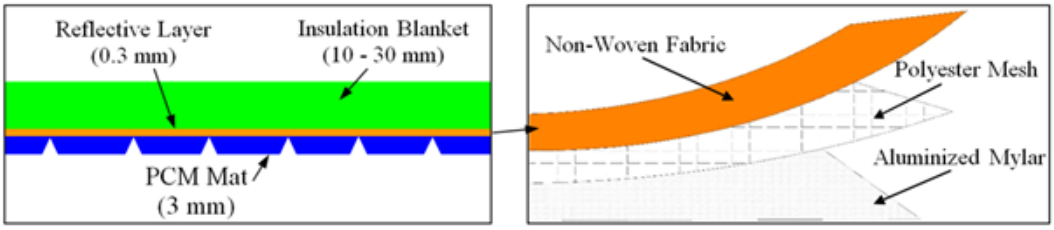

Fig. 2 A schematic representation of the hybrid protection system used at -20ºC

Table 2 Properties of phase change material

Parameter	Value*
Melting point	5°C
Heat storage capacity	187 J/g
Thermal conductivity (liquid/Solid)	0.15/0.25 W/m°C
Density (liquid/Solid)	0.88/0.96 g/ml
Specific heat (liquid/Solid)	2.26/1.78 J/g°C
Number of cycles before instability	10,000 cycles
Expected service life with daily usage	27 years

*Data was provided by the manufacturer.

system (designated as 'IP') as schematically shown in Fig. 2. The PCM melting point is constant at approximately 5ºC (Table 2), thus releasing stored energy (187 J/g) at the cold weather limit defined by ACI 306R (2016) and CSA A23.1 (2019). With PCM, the *R-values* of the supporting insulation blankets were selected at 2.5 and 3.5 (i.e., average of 50% reduction relative to the reference insulation 'I') for curing temperatures of -10 and -20ºC, respectively. At -20ºC, a 0.3 mm reflective layer was attached to the insulation blankets in all cases (i.e., 'I' and 'IP") to improve heat storage at this deep freezing temperature. At the two curing temperatures, the PCM mat in the hybrid system was replaced with another melted one after three and seven days to boost the hydration of the different mixtures.

2.4 Testing

Concrete mechanical properties were assessed based on compressive strength, tensile strength and modulus of elasticity, which were determined by testing triplicate cylinders (100×200 mm) as per ASTM C39 (2020), ASTM C496 (2017) and ASTM C469 (2014), respectively after 28 days of curing under the adopted temperatures and protection methods. In addition, the bond strength of the different mixtures, under different curing temperatures and protection methods, with steel reinforcement at 28 days, were assessed through pull-out tests which were performed on duplicate 200 mm cubic specimens, which were designed following RILEM 7-II-128 (1994) guidelines. Each cube contained a 15M (16 mm) steel re-bar, which had an initial temperatures equal to the curing temperatures (-10 or -20°C), inside concrete cubes with an embedment length of 12.5 times the bar diameter (Fig. 3). Half of the bars embedded length (100 mm) was de-bonded using polyvinyl chloride tubing to reduce the concrete-steel contact area to limit the failure load below the machine loading capacity. Two linear variable displacement transducers (LVDTs) were attached to each specimen to monitor the steel bars free and loaded ends slippage under a constant loading rate of 0.5 kN/s. The LVDTs as well as the machine load were collected using a data acquisition system and used to draw the force-slippage relationships of the different mixtures.

Moreover, the internal temperature of concrete was monitored up to 28 days by Type T thermocouples which were embedded inside the bond test specimens in four different locations; steel-concrete interface, concrete edge, and 1/3 and 2/3 the distance between the concrete edge and steel re-bar, as shown in Fig. 3.

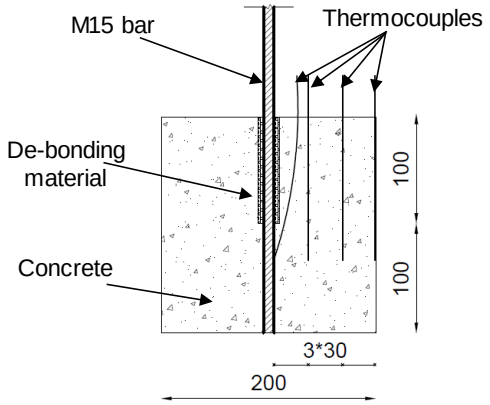

Fig. 3 Schematic drawing of the bond strength specimens (all dimensions are in mm)

To capture the hydration development of binders, thermogravimetry (TG) at 10°C/min constant heating rate was conducted in nitrogen gas environment on powder samples, extracted from the different concrete specimens under the adopted temperatures and protection methods. The portlandite (CH) content of the different mixtures was calculated by multiplying the percentage drop of an ignited mass of the TG curves at the endothermic range of 400 to 450°C by 4.11 (CH-to-water molecular mass) after 1, 3, 7, 14, 28, 56 and 91 days of curing. In addition, the total hydration products at 28 days was expressed by determining the percentage drop of an ignited mass of the TG curves between 105 to 1050°C (Cassagnabère *et al.* 2009). Furthermore, environmental scanning electron microscopy (ESEM) with elemental dispersive X-ray (EDX) analysis were performed on fracture pieces extracted from the interface between steel bars and different concrete specimens after the bond test to capture the effect of changing the mix design parameters and protection methods on the quality of the steel-concrete interfacial transitional zone (ITZ).

3. Model I: Modeling of heat evolution in the assembly

3.1 Theoretical formulation and model parameters

Fundamentally, the heat exchange between two objects, which is governed by the energy conservation and Fourier's laws (Bergman *et al.* 2011, Mills 1999), occurs through one or combinations of three main mechanisms: conduction, convection and radiation. By definition, conduction is the energy transfer between different objects through direct contact, while convection is the transfer of energy through the movement of fluids, whereas the radiation is the energy transfer by electromagnetic emission such as light (Bergman *et al.* 2011, Mills 1999). In this study, the main objective of the thermal modeling was to determine the different elements' heat exchange with surrounding environment due to the conditions imposed on their boundaries. In this case, the heat transfer by convection and

radiation were assumed to be null. Hence, capturing the temperature variation within the assembly (insulation, concrete and steel) is beneficial at defining the temperature of any position at specific time by conduction based on energy conservation and Fourier's laws (Bergman *et al.* 2011, Mills 1999). Assuming a homogeneous medium as well as temperature distribution (T) represented in Cartesian space (x, y, z), the general heat transfer equation, excluding convection and radiation, is determined by the heat flow through the assembly, as expressed in Eq. (1) (Bergman *et al.* 2011, Mills 1999). The right and left hand sides of the equation represent the rate of change in stored energy and energy transferred by conduction, respectively.

$$k\left(\frac{\partial^2 T}{\partial x^2}+\frac{\partial^2 T}{\partial y^2}+\frac{\partial^2 T}{\partial z^2}\right)=C_p\ \rho\ \frac{\partial T}{\partial t} \quad (1)$$

where, K and C_p are the material thermal conductivity (W/m°C) and specific heat capacity (kJ/kg°C), respectively while ρ is its density (kg/m^3).

However, if the material produces heat, such as concrete (through binder reactivity) and PCM, the influence of another term, Q (kJ/m^3) representing the amount of heat generated per unit volume, should be added to the previous equation (Bergman *et al.* 2011, Kim *et al.* 2001, Mills 1999)

$$k\left(\frac{\partial^2 T}{\partial x^2}+\frac{\partial^2 T}{\partial y^2}+\frac{\partial^2 T}{\partial z^2}\right)+Q=C_p\ \rho\ \frac{\partial T}{\partial t} \quad (2)$$

Eq. (2) implies that at any position in the studied assembly, the energy transfer net rate by conduction to the interior of a unit volume in addition to the volumetric rate of thermal energy generation equals to the rate of variation of the thermal energy accumulated inside this volume (Bergman *et al.* 2011, Kim *et al.* 2001, Mills 1999). In case of concrete, the amount of heat generated from binder reactivity can be calculated from Eq. (3)

$$Q\ \left(\frac{kJ}{m^3}\right)=ß\ C_p\ \rho\ (1-e^{\alpha t}) \quad (3)$$

where, t is concrete age (days), while $ß$ and α are constants which were chosen (Tanabe *et al.* 1985) based on binder content, *w/b* as well as the placement temperature.

The finite element modeling was performed based on hourly time steps, then concrete rate of heat generation, $q'$was calculated by Eq. (4)

$$q'\ \left(\frac{kJ}{m^3 h}\right)=\frac{1}{24}ß\ C_p\ \rho\ \alpha\ e^{\frac{\alpha t}{24}} \quad (4)$$

The required parameters to construct the model and thus determine the assembly's temperature gradient are shown in Table 3. For concrete, ρ was determined as per ASTM C138/C138M (2017). The thermal conductivity, k of the different concrete mixtures was calculated using a heat flow meter apparatus (HFMA) as per ASTM C1784 (2020), with an accuracy of ±1% (Russka *et al.* 2017). Slab specimens (200×200×55 mm) were sandwiched between the apparatus plates, which were equipped with a solid state cooling and heating system capable of independently controlling the induced heat flow in either downward or upward direction. Thin (76×76×1.78 mm) heat flux transducers (HFTs) were permanently attached to each of the plates surfaces and a Type E thermocouple was attached to the plates surface, close to the test specimen to monitor the specimen's surface temperature. The plates' temperatures and HFT output were continuously recorded every 1.3 s up to 512 consecutive data points, which were used to calculate the mean plates' temperatures and heat fluxes. According to FOX 314 Instrument Manual (2015), once the thermal equilibrium of the system was achieved (temperature and transducers' signal equilibrium), the thermal properties of concrete were calculated. The thermal diffusivity, δ (m^2/sec) and specific heat, C_p (J/g°C) of concrete were calculated based on Eqs. (5)-(6)

Table 3 Thermal conductivity, specific heat and density input used in the model

Material	Thermal Conductivity, k (W/m°C)	Specific heat, C_p (J/g°C)	Density, ρ (kg/m^3)	Heat Generation (kJ/kg)
Steel Bar[a]	45	502	7800	--
Concrete	By testing	By testing	By testing	Eq. (3)
Plywood[a]	0.12	1210	540	--
PCM[a]	0.20	2	920	187[b]
Reflective Layer[a]	0.01	1000	5	--
Insulation Blanket	0.03	1200	18	--

[a] Data was provided by the manufacturer of each material.
[b] Amount of energy emission when PCM temperature reaches 5°C.

$$\delta=L^2\ \frac{\Delta ln\ Q}{\Delta t\ \pi^2} \quad (5)$$

$$C_p=\frac{k}{\delta\times\rho} \quad (6)$$

where, L is the sample thickness (m), and $\Delta\ ln\ Q/\Delta t$ is the slope of straight line in the graph of natural logarithms of the heat flow signals Q (μV) vs. time t (s).

3.2 Numerical simulation

To capture the effect of changing the mixtures design parameters as well as protection methods on the assembly, twelve 3D (three dimensional) models were created using Ansys 19.2 Workbench platform (2020), with identical dimensions and geometries to laboratory specimens. The software used the finite volume method to solve the partial differential energy equations based on energy conservation and initial conditions of the different elements. To simulate casting and placement conditions, the initial temperature of steel bars and formwork was set to match ambient temperature (-10 or -20°C), while PCM and insulation blankets started at 20°C (brought from storage at room temperature). The concrete mixtures initial temperatures were set based on their placement temperatures after mixing, i.e., 23, 26 and 22°C for single, binary and ternary mixtures, respectively.

The mesh was structured as space discretization by tetrahedral elements with maximum size of 5 mm and average aspect ratio (the measure of mesh element's deviation from having equal lengths of all sides) of 1.87. The different models convergence was defined based on residual energy precision of 6 decimals. Figure 4 shows a general representation of the geometry input of each model. The input material parameters (K, C_p, ρ and Q) were

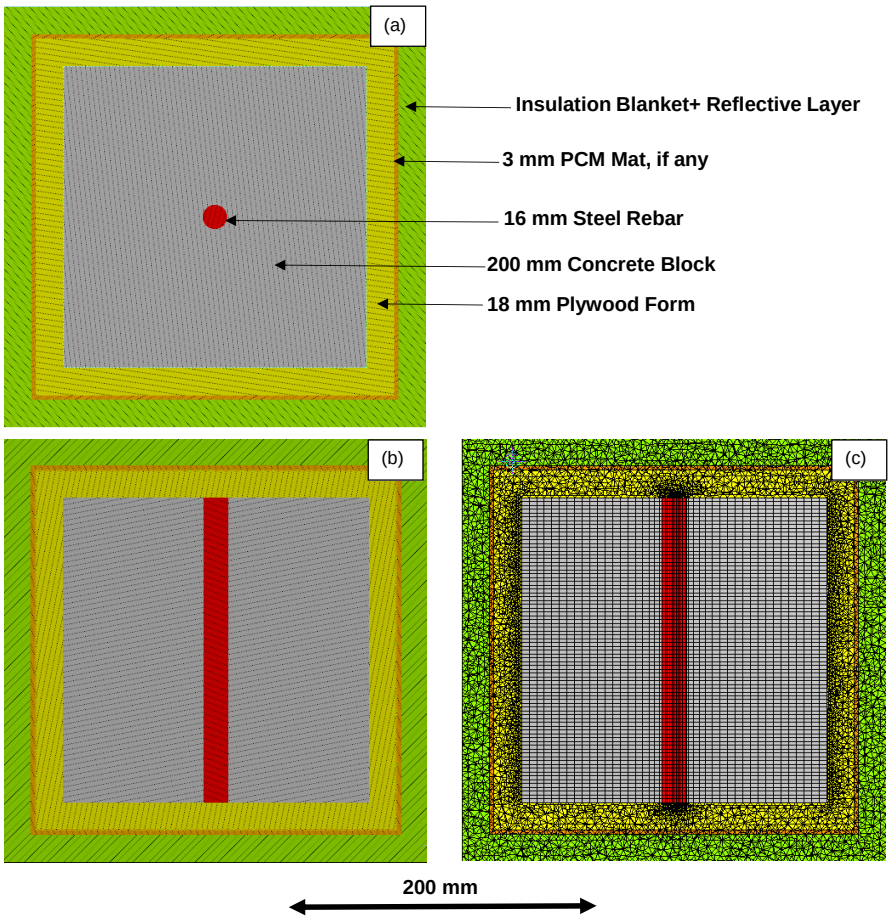

Fig. 4 Finite element geometry of the thermal evolution model: (a) top view; (b) side View; and (c) meshing

identified as per the above description. The presented model output includes temperature gradient of the different assemblies at any time (t) and the final results were presented as net internal heat at the concrete-steel interface after 28 days of curing, Q_{28} (°C-h). This term was integrated with respect to time, representing the area under the temperature-time curve, considering a datum temperature of -10°C, at which the hydration development was negligible based on the phase diagram of the CWAS used (Fig. 1).

4. Model II: Modeling of concrete-steel bonding

4.1 Theoretical formulation and model parameters

The concrete-steel interface behavior under pull-out loading is governed by stress-strain relationships (Yankelevsky *et al.* 2008). Hence, the relative displacement, dl (mm) of a steel bar embedded at distance, dy (mm) in a concrete is equal to the relative displacement of concrete, δ_c (mm) and steel, δ_s (mm) as shown in Eqs. (7)-(8). However, the concrete displacement can be neglected due to its high area and low internal stresses compared to that of steel, and by differentiation of both sides of the equation with respect to dy, Eqs. (9)-(10) can be derived (Yankelevsky *et al.* 2008, Yankelevsky 1985).

$$dl = \delta_s - \delta_c \tag{7}$$

$$dl = \left(\frac{\sigma}{E}\right)_s dy - \left(\frac{\sigma}{E}\right)_c dy \tag{8}$$

$$\frac{dl}{dy} = \left(\frac{\sigma}{E}\right)_s \tag{9}$$

$$\frac{d^2 l}{dy^2} = \left(\frac{1}{E_s}\right) \frac{d\sigma_s}{dy} \tag{10}$$

where, σ and E are internal stress and modulus of elasticity (MPa), while s and c subscripts refer to steel and concrete, respectively.

Hence, the steel and bond stresses over a segment dy are correlated from the equilibrium condition shown in Eq. (11) (Yankelevsky *et al.* 2008, Yankelevsky 1985)

$$(\sigma_s + d\sigma_s)A_s = \sigma_s A_s + \tau\, dy\, \pi\, d \tag{11}$$

Simplifying, Eq. (11) to produce Eq. (12) (Yankelevsky *et al.* 2008, Yankelevsky 1985)

$$\frac{d\sigma_s}{dy} = \tau \left(\frac{\pi\, d}{A_s}\right) \tag{12}$$

By substantiation from Eqs. (10)-(12), the contact surface between the two materials can be modeled analytically by a force-slip relationship which can be simply defined in Eq. (13) (Yankelevsky *et al.* 2008, Yankelevsky 1985) based on the circumferential shear stress, τ (MPa) acting at the contact surfaces between concrete and steel bar

$$\left(\frac{d^2 l}{dy^2}\right) = \tau_y(l_y) \frac{\pi d}{E_s A_s} \tag{13}$$

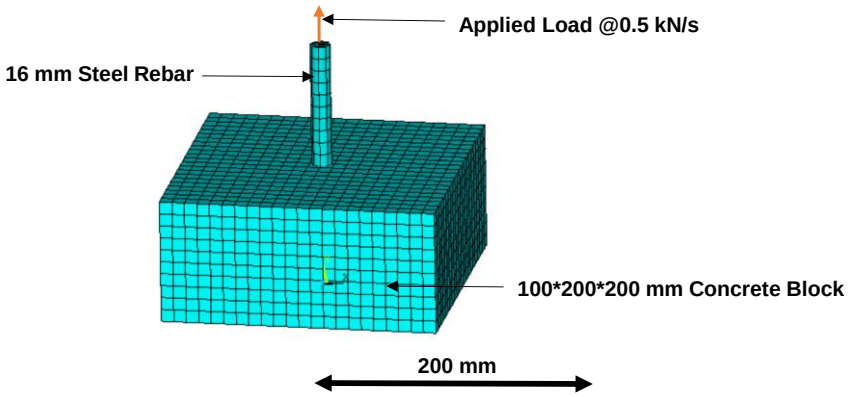

Fig. 5 Geometry of the finite element model for concrete-steel bond

where, τ_y is the shear stress (MPa) , l_y is the slippage (mm) between concrete and steel in y ordinate (direction of loading), while d and A_s are the steel bar diameter (mm) and cross sectional area (mm^2) , respectively.

The input parameters for concrete compressive strength, tensile strength and modulus of elasticity required to construct the model to predict concrete-steel bond strength and plot the force-slip relationship were obtained by testing as mentioned in the Testing section. Concrete Poisson's ratio was assumed as 0.2 for the different concrete mixtures (Neville 2011). The steel bar Poission's ratio, yield and ultimate stresses and modulus of elasticity were input as 0.3, 360 MPa, 520 MPa and 200 GPa, respectively.

4.2 Numerical simulation

Twelve 3D models were developed using Ansys 19.2, Mechanical APDL platform (2019) to predict concrete-steel force-slip relationship. To model the actual bonded length of the steel bar, the cross sectional dimension of the concrete block were kept similar to the actual experimental specimens (200×200 mm) with only 100 mm embedded length, which represents the bonded length with steel bars without sleeve as shown in Fig. 3. The maximum mesh size was 10 mm. The 'Solid65' finite element, which is defined by eight nodes and has isotropic properties, was used to represent concrete blocks in the numerical analysis, while "Beam188" with 16 mm diameter was selected to represent the steel bar. The concrete-steel contact interface was defined using "Combin39", which is a 2-node spring element. Fig. 5 shows a general representation of the geometry of the model.

To simulate the actual testing conditions, the model assembly was constrained in all directions and the steel bar had one degree of freedom in the loading direction. The input parameters of the two materials were integrated into the model, and by applying an axial tension force at a rate of 0.5 kN/s, similar to the experimental loading rate in the direction of the steel bar embedded length, the model generated the force-lip relationship. Hence, the concrete-steel bond strength was determined based on Eq. (14) (Ahmad *et al.* 2018, Yankelevsky 1985)

$$\tau_b = \frac{T}{\pi d L_e} \quad (14)$$

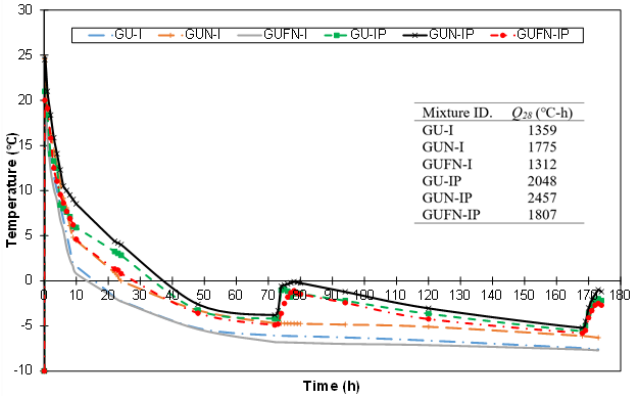

Fig. 6 Internal temperature profiles at the concrete-steel interface in mixtures cured at -10°C during 7 days

where, τ_b is the bond strength (MPa), T is the ultimate failure load (N), d is the steel bar diameter (mm) and L_e is the embedment length in contact with concrete (100 mm).

5. Results and discussion

5.1 Experimental

5.1.1 Internal heat evolution

Figs 6 and 7 present the internal temperature evolution at the concrete-steel interface in specimens during the first 7 days of curing under -10 and -20°C, respectively. Also the net heat produced (Q_{28}), after considering heat generation and losses to adiabatic environment, at this interface in the different mixtures during the first 28 days of curing are tabulated in Figs. 6-7. All steel bars had an initial temperature of -10 or -20°C based on the curing regime (initial condition). After 15 min of casting concrete, the concrete-steel interface temperature increased to reach 20 to 24.5°C due to rapid heat exchange through thermal conduction between the two materials. Afterwards, the interface temperature showed continual drop in all mixtures, which can be ascribed to heat loss to the surrounding environment (-10 or -20°C). Hence, the interface temperature, reached the freezing point of water (0°C) after 14 to 38.5 h and 13 to 26 h and dropped to a range of -5.2 to -7.6°C and -9.2 to -14.1°C, after 7 days of curing at -10 and

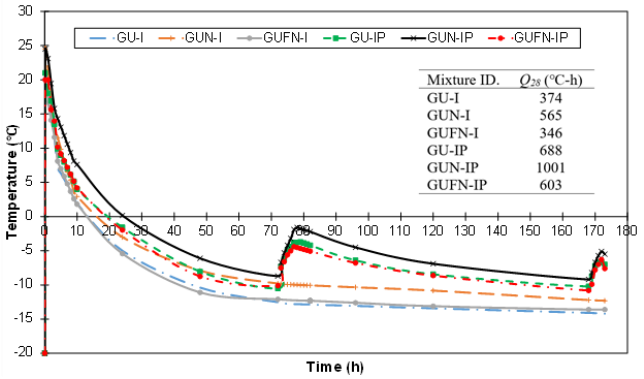

Fig. 7 Internal temperature profiles at concrete-steel interface in mixtures cured at -20°C during 7 days

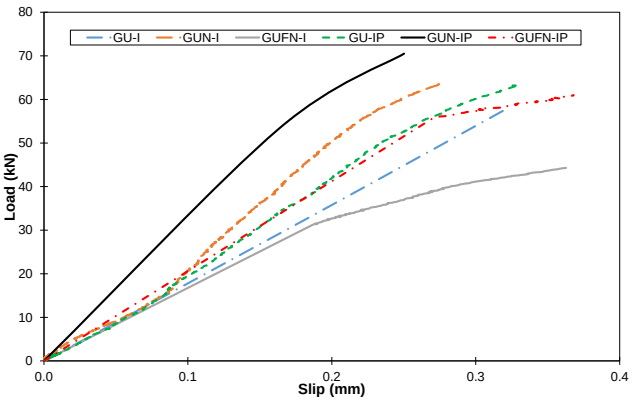

Fig. 8 Load-slip relationship (at the free end) of mixtures after 28 days of curing at -10°C

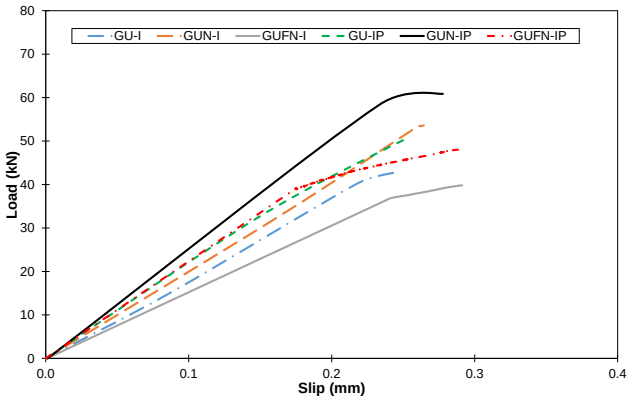

Fig. 9 Load-slip relationship (at the free end) of mixtures after 28 days of curing at -20°C

-20°C, respectively. The different mixtures reached an average minimum temperature of -8.8 to -9.5°C and -17.6 to -19°C after 28 days of curing at -10 and -20°C, respectively, indicating near-equilibrium with adiabatic temperatures irrespective of mix design or protection method.

Although the hybrid protection system had 50% lower *R-values* of insulation compared to the conventional insulation method (refer to the Protection methods section), concrete mixtures protected by the hybrid system showed higher capability of internal heat retention. Hence, after 7 days of curing, the concrete-steel interface temperatures of mixtures protected by the hybrid system were higher (2 to 4°C) compared to the corresponding mixtures protected by the insulation blankets. This can be attributed to the energy release phenomenon of the PCM mat, which re-boosted the reactivity of different binders, resulting in higher internal temperature and Q_{28} as shown in Figs. 6-7. This process was also reflected by the rise (3 to 7°C) at the concrete-steel interface temperature in the different mixtures after 4 to 6 h upon the replacement of the PCM mat after 3 and 7 days of curing. For example, using the hybrid protection method for mixture GU-IP instead of the conventional method led to an average increase in Q_{28} by 51% and 84% at -10 and -20°C curing temperatures, respectively.

Regardless of the protection method and curing temperature, binary mixtures incorporating nano-silica achieved the highest temperatures at the concrete-steel interface. For instance, at -20°C, the temperature of mixture GUN-IP was 2 to 5°C higher than that of the corresponding reference mixture GU-IP during the first 3 days of curing with 45% higher Q_{28} (Fig. 7). This can be linked to nano-silica nucleation and pozzolanic effects on improving the kinetics of binder reactivity, as will be discussed in the Hydration Development section. In contrast, ternary mixtures comprising fly ash with GU and nano-silica experienced higher temperature loss at the concrete-steel interface compared to the corresponding nano-modified binary mixtures. For example, at -10°C, incorporating 20% fly ash in mixture GUN-I to produce mixture GUFN-I reduced Q_{28} by 26%. Nevertheless, the coexistence of nano-silica in the ternary binder partially mitigated the negative effects of fly ash on delaying the internal heat evolution of the binder; hence, the ternary mixtures maintained internal temperatures close to that in the single binders at the concrete-steel interface. For instance, mixture GUFN had an average reduction of 12% and 5% in Q_{28} (Figs. 6-7) compared to that of corresponding mixture GU when protected using the hybrid and conventional methods, respectively at both curing temperatures.

5.1.2 Mechanical properties and bond strength

The force-slip relationships of the different concrete mixtures, cured under both temperatures -10 and -20°C, with steel are shown in Figs. 8-9. Moreover, the mechanical properties, compressive strength (f_c'), tensile (f_t) strength, modulus of elasticity (E), and the bond strength (τ_b), which was calculated based on Eq. (14), of the mixtures after 28 days are shown in Table 4. In the bond test, the splitting failure of concrete was the dominant mode, consequently the bond strength was governed by the mechanical properties of concrete (Butler *et al.* 2011, Gjory *et al.* 1990). ACI 318 (2019) refers to concrete splitting as a mode of failure in multiple sections in Chapter 17 (e.g., sections 17.3.1.1 and 17.4), mainly concerned about anchors. The splitting mode of failure from concrete-steel bond tests has been reported in many research papers (e.g., Chiriatti *et al.* 2019, El-Hacha *et al.* 2006, Lura *et al.* 2002). The bonding failure load of the specimens at 28 days varied between 39.8 to 70.5 kN corresponding to 7.9 to 14 MPa concrete-steel bond strength, which conforms to the bond strength

Table 4 Mechanical properties of concrete and bond strength with steel at 28 days

Mixture ID.	Compressive Strength, f_c' (MPa)	Tensile Strength, f_t (MPa)	Modulus of Elasticity, E (GPa)	Bond Strength, τ_b (MPa)
-10°C Curing Temperature				
GU-I	33.9 (1.3)	3.3 (0.2)	31 (1.5)	11.4 (0.3)
GU-IP	44.7 (2.1)	4.5 (0.2)	41 (1.9)	12.5 (0.5)
GUN-I	39.5 (1.6)	4.7 (0.2)	39 (1.2)	12.7 (0.3)
GUN-IP	51.5 (2.6)	6.1 (0.3)	50 (1.9)	14 (0.3)
GUFN-I	33.1 (1.2)	3.1 (0.1)	29 (1.0)	8.8 (0.2)
GUFN-IP	43.4 (1.5)	4.7 (0.1)	39 (0.8)	12.1 (0.3)
-20°C Curing Temperature				
GU-I	30.1 (1.2)	3.2 (0.1)	27 (1.0)	8.5 (0.1)
GU-IP	34.6 (1.8)	3.5 (0.2)	32 (0.9)	10.1 (0.2)
GUN-I	35.6 (1.4)	3.7 (0.2)	32 (1.2)	10.7 (0.1)
GUN-IP	45.0 (2.2)	5.0 (0.1)	42 (2.0)	12.1 (0.4)
GUFN-I	29.3 (0.9)	3.4 (0.2)	27.5 (0.8)	7.9 (0.2)
GUFN-IP	33.6 (1.3)	3.6 (0.1)	32 (1.0)	9.6 (0.3)

Note: numbers in parentheses represent standard deviations.

values for concrete with similar strength grade and re-bar size, but cast and cured under normal temperatures (Bahekar and Gadve 2019, Diab *et al.* 2014). Bond strength of concrete is governed by the mode of failure which is a function of concrete confinement, mechanical interaction, friction, and chemical adhesion with steel re-bars (Gjory *et al.* 1990). When the re-bar embedded length is high enough, the splitting mode of failure of concrete dominates the bond test due to surrounding concrete failure by cracking (Gjory *et al.* 1990), which is affected by the degree of hydration of the cementitious matrix. This is prudent to the current case to substantiate the evolution of mechanical properties of the mixtures, under different freezing temperatures and protection methods, with respect to bonding with steel.

Changing the protection method had a marked effect on the mechanical properties and in turn bond strength of concrete mixtures cured at both freezing temperatures. Accordingly, concrete mixtures protected by the hybrid system achieved higher bond strength than that of similar concrete covered with conventional insulation by an average of 18% at both curing temperatures. This conformed to the higher compressive strength, tensile strength and modulus of elasticity of mixtures protected using the hybrid system compared to that of similar concrete protected by the conventional method. For instance, after 28 days of curing at -20°C, mixture GU-IP achieved 10, 32, 36 and 32% higher bond, compressive and tensile strengths and modulus of elasticity, compared to that of mixture GU-I. This complies with the higher internal heat of mixtures protected by the hybrid system, indicating better development in paste microstructure and ITZ with steel bars as will be discussed in the subsequent section.

Irrespective of the curing temperature and protection method, nano-modified concrete (binary mixtures) achieved the highest mechanical properties. For example, at -20°C, incorporating 6% nano-silica in mixture GU-IP to produce mixture GUN-IP increased the bond, compressive, and tensile strengths and modulus of elasticity by 20, 30, 43,

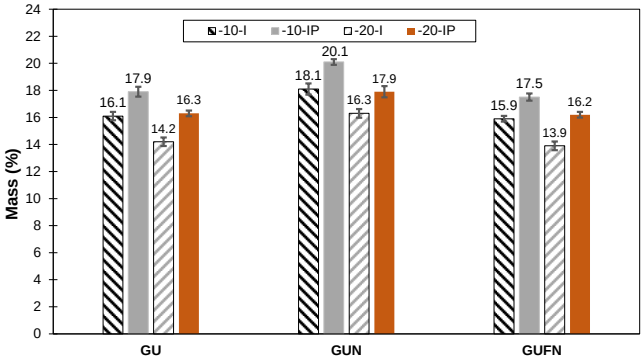

Fig. 10 Mass of hydration products in mixtures at 28 days. (Note: error bars represent standard deviations)

and 31% respectively. Comparatively, Class F fly ash, which is a slowly reactive pozzolan, has a well-documented delaying effect on the development of concrete mechanical properties at 28 days under normal and low temperatures down to -5°C (Yasien *et al.* 2019, Abayou *et al.* 2019, Neville 2011). Albeit this effect would be expected to exacerbate under the freezing regimes (-10/-20°C) adopted herein, the coexistence of nano-silica in mixtures comprising fly ash alleviated this negative effect on concrete, regardless of the protection method. Hence, ternary mixtures comprising nano-silica and fly ash yielded mechanical properties close to the corresponding single binder mixtures. For example, at -20°C, the incorporation of 6% nano-silica and 20% fly ash in mixture GU-IP to produce mixture GUFN-IP led to marginal reduction in bond and compressive strengths by 5% and 3%, respectively with 3% increase in tensile strength and similar modulus of elasticity at 28 days.

5.1.3 Hydration development and microstructure characteristics

Fig. 10 shows the mass of hydration products after 28 days of curing under -10 and -20°C. The different mixtures showed continual hydration, despite the gradual drop in internal temperature that reached 0°C after 13 to 38.5 h of curing, as discussed in the previous section. Mixtures protected using the hybrid system achieved 12% average increase in the mass of hydration products compared to corresponding mixtures protected using the conventional method, which complies with enhanced performance of mixtures protected using the hybrid system.

Fig. 11 shows exemplar portlandite (calcium hydroxide, CH) trends in some mixtures up to 91 days. It supports the superior performance of mixtures comprising nano-silica due to its vigorous reactivity associated with its ultra-fineness, as nano-modified mixtures (GUN-IP at -10 and -20°C) produced higher CH contents at early-age. This can be ascribed to the nucleation effects of nano-silica on the kinetics of cement hydration at early-age by providing the hydration products with additional surfaces to precipitate on (Madani *et al.* 2012), even under low temperatures. Indeed, the coexistence of CWAS (accelerating/anti-freeze admixture) kept the functionality of nano-silica, under the freezing temperatures adopted herein. This conforms to the higher internal heat of binary binder mixtures compared to

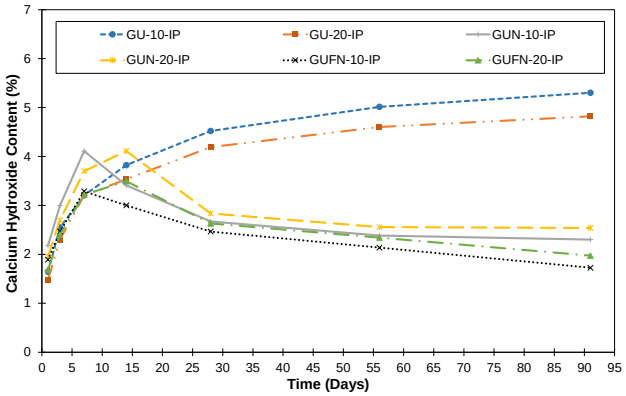

Fig. 11 Exemplar thermogravimetry results for the portlandite contents in some mixtures up to 91 days of curing

that of single binder mixtures. In addition, the nano-modified mixtures showed consumption of CH after 7 and 14 days of curing at -10 and -20°C, respectively, indicating the initiation of delayed pozzolanic reactivity by reacting with CH to produce secondary C-S-H gel. This pozzolanic reactivity was accompanied by the filler effect in the matrix (Yasien *et al*. 2019, Abayou *et al*. 2019, Ghazy *et al.* 2016, Madani *et al.* 2012), which explains the marked improvement in mechanical properties, including bond strength with steel re-bars, of these mixtures at 28 days. This corresponded to higher mass (average of 12% higher) of hydration products in nano-modified mixtures at 28 days compared to that in single binder mixtures (Fig. 10).

Likewise, the mass of hydration products (Fig. 10) in ternary mixtures were 14% lower than that in binary mixtures but comparable to that in the single binder mixtures. Furthermore, as shown in Fig. 11, ternary mixtures showed continual hydration development, even with the existence of 20% Class F fly ash, due to the synergistic effects of nano-silica and CWAS which catalyzed the indolent reactivity of fly ash. Hence, nano-modified fly ash concrete, cast and cured under freezing temperatures down to -20°C showed acceptable performance in terms of hydration development and mechanical properties. This highlights that ACI 306R (2016) and CSA A23.1 (2019) recommendations against the use of slow reactivity supplementary cementitious materials in cold weather concreting can be mitigated by the addition

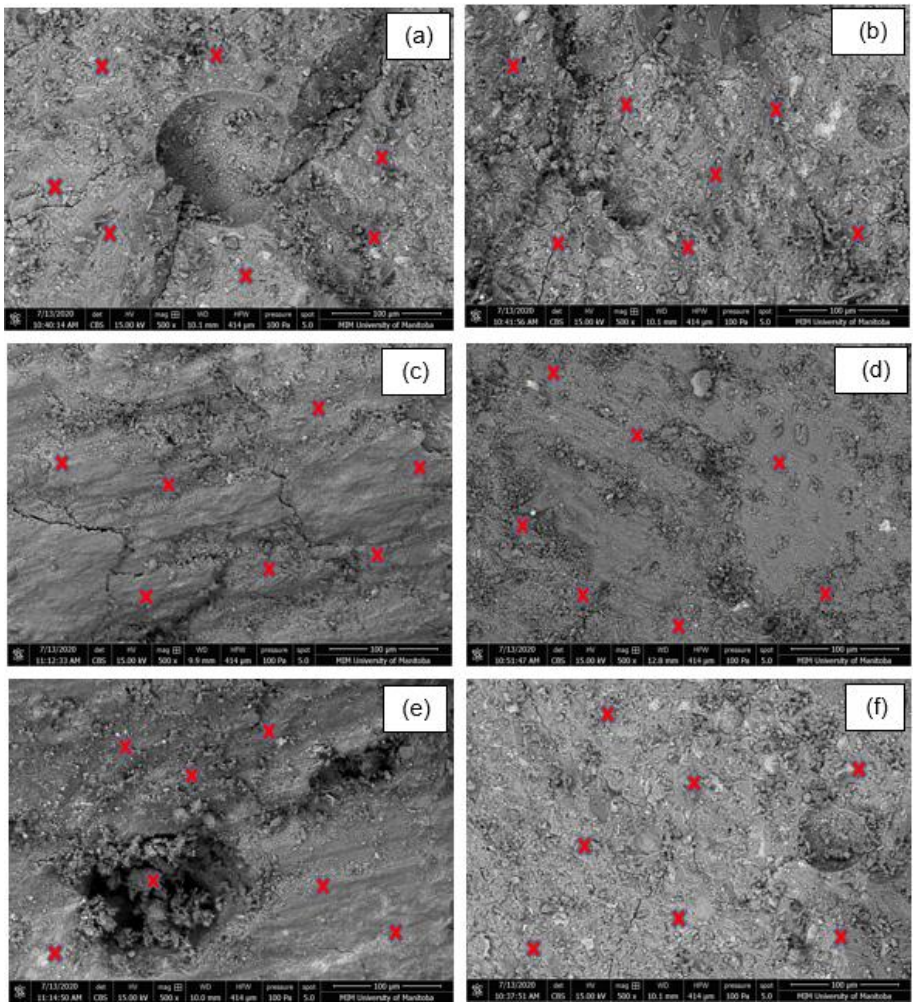

Fig. 12 Exemplar ESEM micrographs for mixtures cured at -10°C: (a) GU-I (avg. *C/S*=1.8), (b) GU-IP (avg. *C/S*=1.6), (c) GUN-I (avg. *C/S*=1.3), (d) GUN-IP (avg. *C/S*=1.1), (e) GUFN-I (avg. *C/S*=1.7), and (f) GUFN-IP (avg. *C/S*=1.4). Note: The *C/S* was calculated based on the marked locations

of nano-silica.

To corroborate the findings from the TG test, exemplar mixtures were selected to perform ESEM on fracture pieces extracted from the concrete-steel interface in specimens after the bond test (Fig. 12). In addition, the average calcium-to-silicate ratio (*C/S*) within the concrete-steel ITZ was determined by EDX, which was performed at multiple points. Detwiler *et al.* (1996) reported that the *C/S* of secondary/pozzolanic and conventional C-S-H were approximately 1.1 and 1.7, respectively. The microstructural features of the different mixtures were dissimilar, which indicated the dominant effect of changing the mix design and/or protection method on concrete cast and cured at the freezing temperatures adopted herein. It is worth noting that the micro-cracks appearing in the images are associated with mechanical loading during the pull-out test which led to concrete failure as will be discussed in Model II results.

Complying with the previous findings, mixtures protected using the hybrid system produced denser cementitious matrix than that of similar mixtures protected by the conventional method (Figs. 12 (b)-(d)-(f) vs. Figs. 12 (a)-(c)-(e)). This can be attributed to the heat release phenomenon of the PCM mat, which has a latent energy storage process. The PCM mat acted as a sustainably external heat source by emitting thermal energy at a rate of 187 kJ/kg in the hybrid system through its solidification process from the liquid state at 5ºC. This explains the relatively higher internal concrete-steel interface temperature of mixtures protected by the hybrid system. Consequently, it maintained concrete hydration development rate at higher level compared to the conventional protection method. This led to better cementitious matrix quality, lower *C/S* and improved ITZ with steel bars, and consequently higher mechanical bonding.

The inclusion of nano-silica in concrete cast and cured under freezing temperatures adopted herein produced more homogenous microstructure, regardless of the protection method. For instance, the incorporation of 6% nano-silica in mixture GU-I to produce mixture GUN-I reduced the *C/S* from 1.8 to 1.3 as shown in Figs. 12 (a)-(c), respectively, which highlights the pronounced effect of nano-silica pozzolanic reactivity, even under freezing temperatures, on densifying concrete-steel ITZ by producing secondary C-S-H gel, which improved the bond strength of the binary binder mixtures. Accordingly, as shown in Fig. 12 (e) and (f), the negative effects of incorporating 20% slowly reactive material such as Class F fly ash was alleviated by the co-existence of nano-silcia. Hence, nano-modified fly ash mixtures showed better microstructure characteristics (densified concrete-steel ITZ) and lower (*C/S*) compared to single binder mixtures, especially when protected using the hybrid system. This supports the previously discussed synergistic effect of nano-silica and fly ash which produced concrete mixtures with comparable/ better performance than the corresponding single binder mixtures.

5.2 Modeling

5.2.1 Model I: Thermal model

Table 5 lists the thermal conductivity (k), specific heat (C_p) and density (ρ) input values for the different mixtures at both curing temperatures. While Figs. 13-14 show the predicted temperature-time profiles up to 7 days as well as the predicated Q_{28} at the interface of the concrete-steel in the assembly based on the numerical results for both curing temperatures. The temperature profiles and net heat values were in good agreement with the experimental results (Figs. 6-7). For example, at -10°C, the predicted Q_{28} values of single, binary and ternary mixtures protected using the conventional method were 1302, 1702 and 1236°C-h, respectively corresponding to experimental values of 1359, 1775 and 1312°C-h, respectively. The thermal stratification from the models (e.g., Figs. 15-16) at a horizontal plane located in the middle of the assembly conformed to the previously discussed effects of changing the protection method and mix design on the internal temperature evolution of concrete.

Table 5 Average values of thermal conductivity, specific heat and density used in Model I

Mixture ID.	Thermal Conductivity, k (W/m°C)	Specific heat, C_p (J/g°C)	Density, ρ (kg/m^3)
-10°C Curing Temperature			
GU-I	1.37	870	2270
GU-IP	1.27	948	2315
GUN-I	1.22	1001	2305
GUN-IP	1.14	1050	2350
GUFN-I	1.38	857	2245
GUFN-IP	1.3	911	2300
-20°C Curing Temperature			
GU-I	1.56	852	2170
GU-IP	1.39	878	2205
GUN-I	1.41	933	2210
GUN-IP	1.31	971	2250
GUFN-I	1.63	845	2150
GUFN-IP	1.47	867	2190

The developed models were used to predict the time required to melt any ice lensing at the concrete-steel interface, which might negatively affect the concrete-steel bonding. The judgement criterion adopted herein was to increase the internal temperature of the outer surface of the steel re-bars, which is in contact with freshly placed concrete, to above 0°C. It was found that only a thin crust (1 to 2 mm) of concrete around the unheated steel re-bar was affected by the thermal difference between both materials. Regardless of the mix design or the protection method, the time required to reach above 0°C in this curst was very rapid between 17 and 37 s for both curing regimes. This highlights that efficient winter concrete mixture designs, especially the ones comprising nano-silica, incorporating CWAS and protected using the proposed systems can be cast against metallic embedments (up to 200 mm^2) with an initial temperature down to -20°C without the need for any heating procedures. This alleviates ACI 306R (2016) requirements, which recommends to heat any metallic embedments in contact with concrete when the ambient temperature is below -12°C.

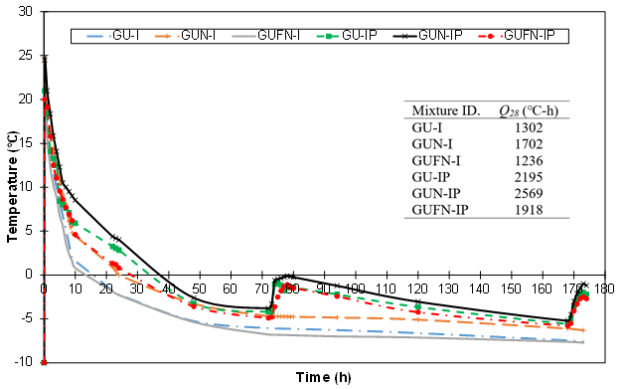

Fig. 13 Predicted temperature profiles at concrete-steel interface in mixtures cured at -10°C up to 7 days

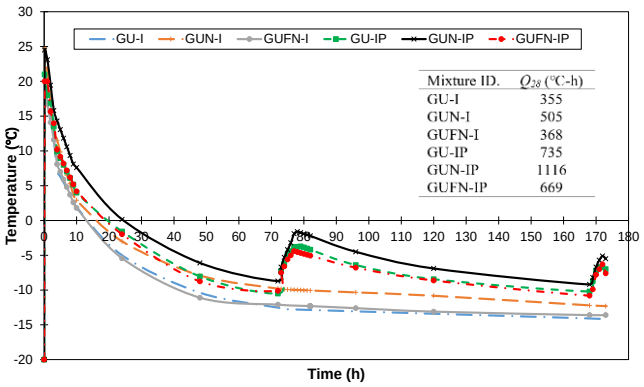

Fig. 14 Predicted temperature profiles at concrete-steel interface in mixtures cured at -20°C up to 7 days

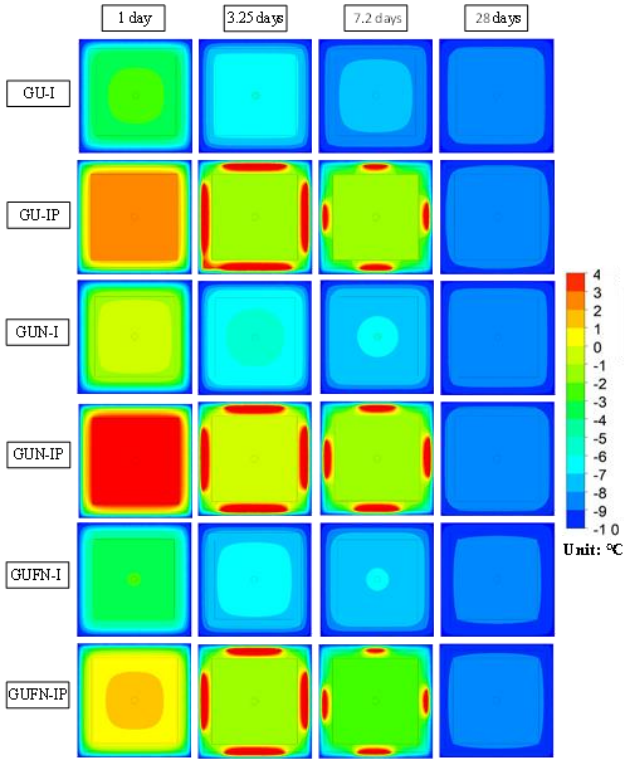

Fig. 15 Temperature stratification with respect to time in different mixtures cured under -10°C

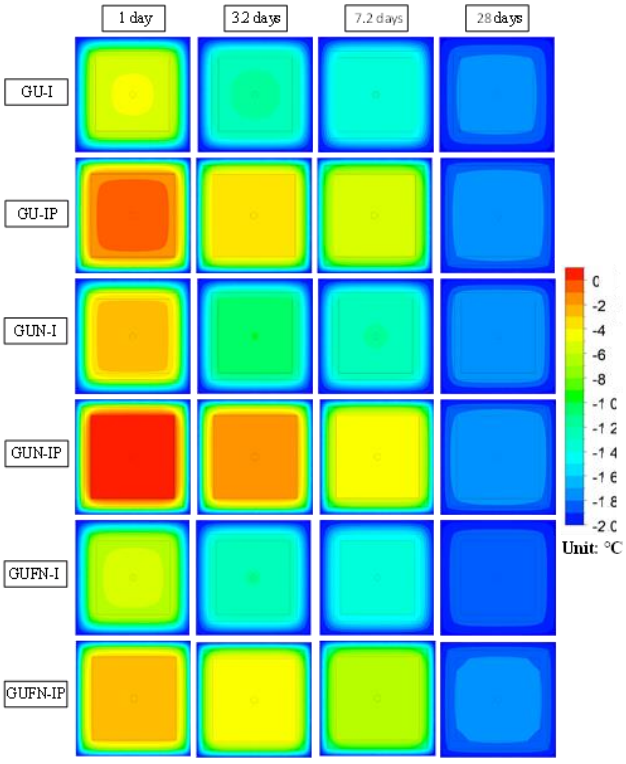

Fig. 16 Temperature stratification with respect to time in different mixtures cured under -20°C

5.2.2 Model II: Bonding model

The model input parameters are compressive (f_c'),tensile strengths (f_t) and modulus of elasticity (E) which were obtained experimentally (Table 4). To eliminate the need for performing lab tests to run the concrete-steel bonding finite element model, a nomogram (Fig. 17) was also developed by implementing regression analysis to correlate Q_{28}, (output of the thermal model), mass of hydration products at 28 days and the mechanical properties of concrete based on the results of the previous sections. The nomogram consists of three parts: the bottom part represents the relationship between Q_{28} and hydration products content (%), in the range of the curing temperatures adopted herein, the top right part correlates between the hydration products content (%) and 28 day compressive strength of concrete (f_c'), while the top left part links the latter parameter to both tensile strength (f_t) and modulus of elasticity (E) of concrete. Exponential, power and linear correlations were established among the different parameters with high coefficients of determination (R^2) (0.95 to 0.97), indicating that the predicted properties varied systematically with experimentation. Thus, using the output of thermal modeling, the mechanical parameters needed for the bond strength predictions can be directly obtained from the nomogram, as for example shown by the guideline arrows in Fig. 17.

Figs. 18 and 19 present the predicted force-slip relationships as well as the bond strength (τ_b) of the different mixtures cured at -10 and -20°C, respectively. The predictions conformed to the experimental trends. For instance, at -10°C, the model predicted τ_b values of the single, binary and ternary mixtures protected by the hybrid

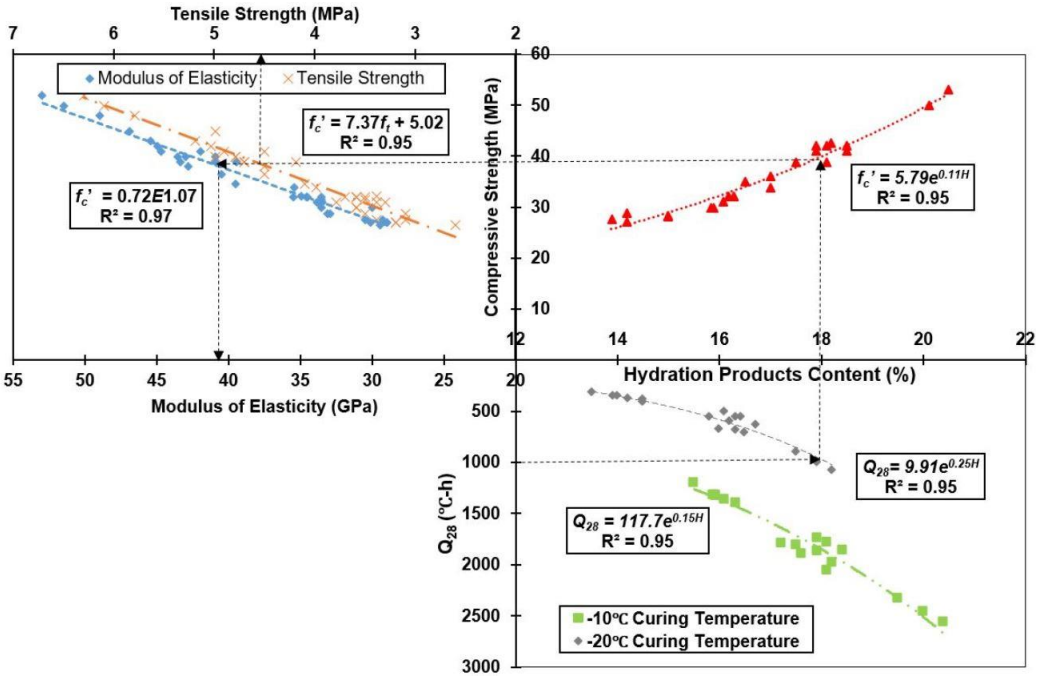

Fig. 17 Nomogram correlating the net heat from the thermal model (Q_{28}) to content of hydration products (H) and mechanical properties at 28 days for concrete cast and cured under freezing temperatures

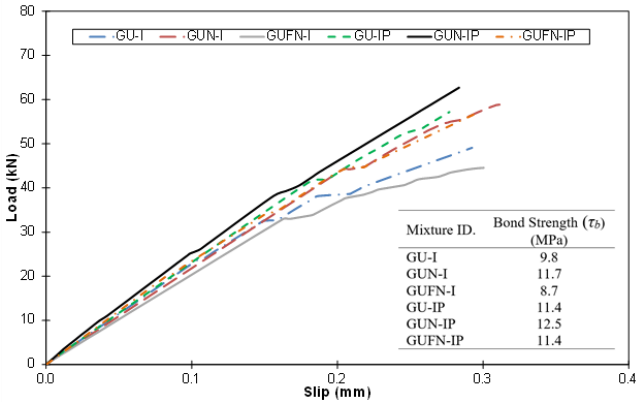

Fig. 18 Predicted load-slip relationship of concrete mixtures cured at -10°C

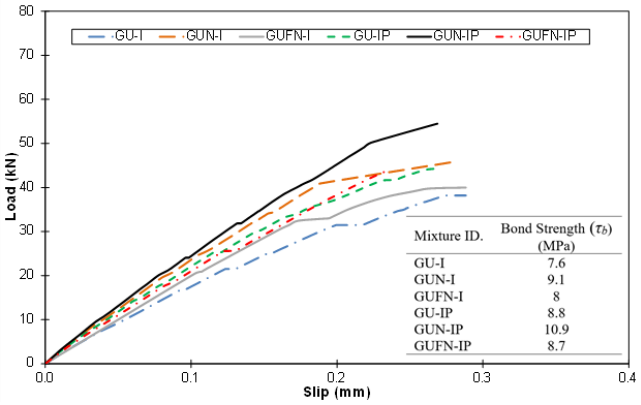

Fig. 19 Predicted load-slip relationship of concrete mixtures cured at -20°C

system as 11.4, 12.5 and 11.4 MPa in comparison with 12.5, 14 and 12.1 MPa from the experimental results, respectively. The differences between the numerical and experimental bond strength results can be linked to the fact that numerical model was based on solving the mathematical equations, described in the numerical simulation section, and thus the results will be affected by assumptions such as linearity of stress and strain distributions. On the other hand, experimental results are affected by multiple factors including nonlinearity of the actual material behavior, errors in devices and instrumentation, specimens' deficiencies and potential eccentricity of re-bars. Nevertheless, the accuracy of the bonding model was acceptable as will be shown in the subsequent section. The numerical results indicated the same trends observed in the laboratory with respect to concrete-steel bonding. Mixtures protected using the hybrid system achieved higher bond strength compared to that of similar mixtures protected using the conventional method. Moreover, nano-modified binary mixtures achieved the highest bond strength while ternary mixtures showed comparable bond strength to that of single binder mixtures, under similar curing temperatures and protection methods.

In addition, the developed models simulated cracking of concrete and mode of failure. As shown in Figs. 20 (a)-(b), the model suggested that the first-crack patterns, representing failure of concrete as the induced principle stresses reached capacity of concrete, were mainly perpendicular and parallel to the loading direction. In Fig. 20(a), the cracks propagated perpendicular to the loading direction (circles represent cracks propagation direction) due to the wedging action of the steel bar; thus the bond forces were directed outward from the bar surface resulting in tensile stresses higher than concrete tensile strength. Then, as shown in Fig. 20(b), these cracks propagated vertically (circles crossed with vertical lines) along the

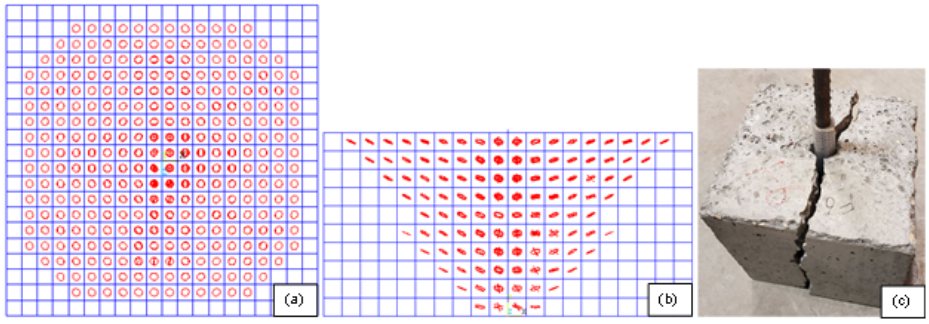

Fig. 20 Exemplar cracking patterns at the failure load of mixture GUFN-IP cured at -20°C: (a) top view, (b) side view, and (c) experimental mode of failure

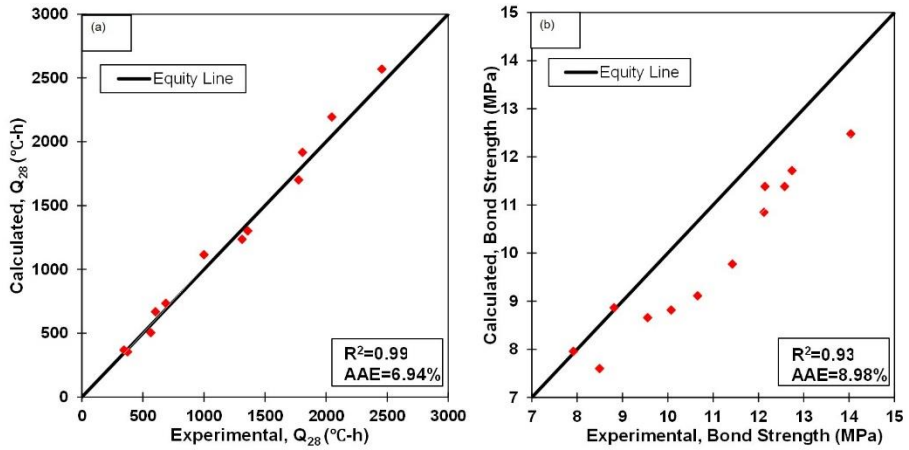

Fig. 21 Response of numerical models to predict the 28 day: (a) net heat (Q_{28}), (b) bond strength (τ_b)

depth of concrete block leading to anchorage failure and concrete splitting (Butler *et al.* 2011, Gjory *et al.* 1990), which was the dominant mode of failure in this study (Fig. 20(c)).

5.2.3 Models' performance

Figs. 21(a)-(b) show the numerical models output to predict Q_{28} and τ_b, respectively relative to their corresponding experimental values. For the thermal model, the points were located primarily on the line of equity or in the vicinity of this line. However, the datasets were mostly skewed under the line of equity for the bonding model, indicating that the numerically predicted bond strength values were conservative. Moreover, the performance of models was evaluated by calculating the average absolute error (AAE), which is the average magnitude of errors, according to Eq. (15) (Montgomery 2017) to quantify the accuracy of calculated values from the models relative to the measured ones. The AAE for the thermal and bond models were 6.94% and 8.98%, respectively and the corresponding R^2 (Eq. (16)) (Montgomery 2017) values were of 0.99 and 0.93, respectively. This indicated strong association between the predicted and experimental data sets (less than 10% error), which substantiated the reasonableness of the assumptions, parameters and algorithms adopted to establish the thermal and bonding models.

$$AAE = \frac{100}{n_d}\sum_{i=1}^{n}\frac{|x-y|}{x} \quad (15)$$

$$R^2 = \left(\frac{n_d(\sum xy)-(\sum x)(\sum y)}{\sqrt{[n_d\ \sum x^2-(\sum x)^2]\ [n_d\ \sum y^2-(\sum y)^2]}}\right)^2 \quad (16)$$

where, n_d is the total number of data points, while x and y are the experimental and predicted values, respectively.

The models presented herein can be beneficially used for similar field concrete mixtures cast and cured under similar freezing conditions. Since, the accuracy of the models was high, the developed thermal model may have an adequate generalization capacity to predict concrete-steel interface temperature evolution, which can be used to calculate the net heat (Q_{28}), and corresponding degree of hydration and mechanical properties of concrete from the nomogram developed in Fig. 17. Subsequently, these mechanical properties can be integrated into the bonding model to project the concrete-steel force-slip relationship to estimate the bond strength (τ_b) of the assembly.

6. Conclusions

Considering the mixture designs, mixing/curing temperatures, protection and test methods as well as the numerical simulations implemented in this study, the following conclusions can be drawn:

- Without heating, the hybrid protection system (reduced *R-values* insulation+PCM mat) produced concrete mixtures with improved mechanical properties and bond strength with steel compared to the conventional method (higher *R-values* insulation). The PCM acted as a

renewably external curing aid through its heat release phenomenon, which improved the hydration and microstructure development of concrete cast and cured under both freezing temperatures (-10 and -20°C).

• The results of bulk tests yielded high coefficients of determination ($R \approx 0.95$) among concrete internal net heat (Q_{28}), mass of hydration products, compressive strength (f_c'), tensile strength (f_t) and modulus of elasticity (E) after 28 days of curing at both freezing temperatures.

• The developed thermal analysis model has an adequate generalization capability to predict concrete-steel interfacial temperature evolution, which can be used to calculate the net heat (Q_{28}), consequently concrete mechanical properties (f_c', f_t, and E) can be predicted using the established nomogram. These properties can be integrated into the bonding model as input parameters to determine concrete-steel force-slip relationship, bond strength (τ_b) as well as concrete cracking pattern. The proposed models produced accurately predicted concrete behavior thermally and mechanically with less than 10% error between predicted and experimental results.

• The quality of ITZ between concrete and steel was implicated in the numerical modeling of bulk properties by considering the Q_{28} which proved to have a good correlation with the degree hydration of the cement paste, and concrete engineering properties needed to predict concrete-steel bond strength. Yet, the ITZ characteristic at micro- or nano-scale, can be further assessed by refined modeling and verified by sophisticated experimental techniques such as nano-indentation, which is recommend for future research.

• The synoptic experimental and numerical results herein showed that nano-modified concrete comprising CWAS, without or with fly ash (20%) and protected using the hybrid system achieved adequate hydration development, mechanical properties and bonding with steel re-bars due to the nucleation, pozzolanic and filler effects of nano-silica.

• The integrated strategy of nano-modified concrete and hybrid protection system presents a viable option to produce reinforced concrete elements suitable for cold weather applications down to -20°C without the need for heating practices. This still needs to be further substantiated by field trials on large-scale elements, in addition to investigating the effect of increasing the re-bar diameter and concrete cover on concrete Q_{28}, τ_b as well as mode of failure, which are recommended for future research.

Acknowledgement

The authors highly appreciate the financial support from Natural Sciences and Engineering Research Council of Canada and University of Manitoba Graduate Fellowship and GETS program. The IKO Construction Materials Testing Facility at the University of Manitoba, in which these experiments were conducted.

References

Abayou, A., Yasien, A. and Bassuoni, M. (2019), "Properties of nanosilica-modified concrete cast and cured under cyclic freezing/low temperatures", *Adv. Civil Eng.*, **8**(3), 287-306. https://doi.org/10.1520/ACEM20190013.

ACI-306R (2016), Guide to Cold Weather Concreting, American Concrete Institute, Farmington Hills, Michigan.

ACI-318 (2019), Building Code Requirements for Structural Concrete, American Concrete Institute, Farmington Hills, Michigan.

Aguayo, M., Das, S., Maroli, A., Kabay, N., Mertens, J.C., Rajan, S.D., Sant, G., Chawla, N. and Neithalath, N. (2016), "The influence of microencapsulated phase change material (PCM) characteristics on the microstructure and strength of cementitious composites: Experiments and finite element simulations", *Cement Concrete Compos.*, **73**, 29-41. https://doi.org/10.1016/j.cemconcomp.2016.06.018.

Ahmad, S., Pilakoutas, K., Rafi, M.M. and Zaman, Q.U. (2018), "Bond strength prediction of steel bars in low strength concrete by using ANN", *Comput. Concrete*, **22**(2), 249-259. https://doi.org/10.12989/cac.2018.22.2.249.

ANSYS Inc. (2019), Ansys Mechanical Apdl Verification Manual 2019R3, Pennsylvania, United States.

ANSYS Inc. (2020), Ansys Fluent Theory Guide 2020R1, Pennsylvania, United States.

ASTM C138/C138M (2017), Standard Test Method for Density (unit weight), Yield, and Air Content (gravimetric) of Concrete, American Society for Testing and Materials, West Conshohocken, PA, USA.

ASTM C1784 (2020), Measuring Thermal Conductivity and Specific Heat Capacity Values of Inhomogeneous Materials with a Heat Flow Meter Apparatus, American Society for Testing and Materials, West Conshohocken, PA, USA.

ASTM C260/C260M (2016), Standard Specification for Air-Entraining Admixtures for Concrete, American Society for Testing and Materials, West Conshohocken, PA.

ASTM C39/C39M (2020), Standard Test Method for Compressive Strength of Cylindrical Concrete Specimens, American Society for Testing and Materials, West Conshohocken, PA, USA.

ASTM C469/C469M (2014), Standard Test Method for Static Modulus of Elasticity and Poisson's Ratio of Concrete in Compression, American Society for Testing and Materials,West Conshohocken, PA, USA.

ASTM C494/C494M (2019), Standard Specification for Chemical Admixtures for Concrete, American Society for Testing and Materials, West Conshohocken, PA, USA.

ASTM C496/C496M (2017), Standard Test Method for Splitting Tensile Strength of Cylindrical Concrete Specimens, American Society for Testing and Materials, West Conshohocken, PA, USA.

Baetens, R., Jelle, B.P. and Gustavsen, A. (2010), "Phase change materials for building applications: a state-of-the-art review", *Energy Build.*, **42**(9), 1361-1368. https://doi.org/10.1016/j.enbuild.2010.03.026.

Bahekar, P.V. and Gadve, S.S. (2019), "Corrosion of rebar in carbon fiber reinforced polymer bonded reinforced concrete", *Adv. Concrete Constr.*, **8**(4), 247-255. https://doi.org/10.12989/acc.2019.8.4.247.

Barna, L.A., Seman, P.M. and Korhonen, C.J. (2011), "Energy-efficient approach to cold-weather concreting", *J. Mater. Civil Eng.*, **23**(11), 1544-1551. https://doi.org/10.1061/(ASCE)MT.1943-5533.0000262.

Bergman, T.L., Incropera, F.P., DeWitt, D.P. and Lavine, A.S. (2011), *Fundamentals of Heat and Mass Transfer*, John Wiley & Sons, New Jersey, United States.

Butler, L., West, J.S. and Tighe, S.L. (2011), "The effect of recycled concrete aggregate properties on the bond strength between RCA concrete and steel reinforcement", *Cement Concrete Res.*, **41**(10), 1037-1049. https://doi.org/10.1016/j.cemconres.2011.06.004.

Cao, V.D., Pilehvar, S., Salas-Bringas, C., Szczotok, A.M., Rodriguez, J.F., Carmona, M., AL-Manasir, N. and Kjøniksen, A.L. (2017), "Microencapsulated phase change materials for enhancing the thermal performance of Portland cement concrete and geopolymer concrete for passive building applications", *Energy Convers. Manage.*, **133**, 56-66. https://doi.org/10.1016/j.enconman.2016.11.061.

Cassagnabère, F., Mouret, M. and Escadeillas, G. (2009), "Early hydration of clinker–slag–metakaolin combination in steam curing conditions, relation with mechanical properties", *Cement Concrete Res*., **39**(12), 1164-1173. https://doi.org/10.1016/j.cemconres.2009.07.023.

Chiriatti, L., Mercado-Mendoza, H., Apedo, K.L., Fond, C. and Feugeas, F. (2019), "A study of bond between steel rebar and concrete under a friction-based approach", *Cement Concrete Res*., **120**, 132-141. https://doi.org/10.1016/j.cemconres.2019.03.019.

CS164 (2016), Concrete Practice: Guidance on the Practical Aspects of Concreting, The Concrete Society, Good Concrete Guide 8, Camberley, United Kingdom.

CSA-A23.1/A23.2 (2019), Concrete Materials and Methods of Concrete Construction/Test Methods and Standard Practices for Concrete, Canadian Standards Association, Mississauga, ON, Canada.

CSA-A3001 (2018), Cementitious Materials for Use in Concrete, Canadian Standards Association, Mississauga, ON, Canada.

Detwiler, R., Bhatty, J. and Bhattacharja, S. (1996), *Supplementary Cementing Materials for Use in Blended Cements*, Portland Cement Association, Skokie, IL, USA.

Diab, A.M., Elyamany, H.E., Hussein, M.A. and Al Ashy, H.M. (2014), "Properties of pull-out bond strength and concept to assess ultimate bond stress of NSC and HSC", *Mag. Concrete Res*., **66**(17), 877-895. https://doi.org/10.1680/macr.14.00009.

Dorigato, A., Canclini, P., Unterberger, S.H. and Pegoretti, A. (2017), "Phase changing nanocomposites for low temperature thermal energy storage and release", *Express. Polym. Lett.*, **11**(9), 738-752.

El-Hacha, R., El-Agroudy, H. and Rizkalla, S.H. (2006), "Bond characteristics of high-strength steel reinforcement", *ACI Struct. J*., **103**(6), 771.

Farnam, Y., Krafcik, M., Liston, L., Washington, T., Erk, K., Tao, B. and Weiss, J. (2015), "Evaluating the use of phase change materials in concrete pavement to melt ice and snow", *J. Mater. Civil Eng.*, **28**(4), 04015161. https://doi.org/10.1061/(ASCE)MT.1943-5533.0001439.

Fernandes, F., Manari, S., Aguayo, M., Santos, K., Oey, T., Wei, Z., Falzone, G., Neithalath, N. and Sant, G. (2014), "On the feasibility of using phase change materials (PCMs) to mitigate thermal cracking in cementitious materials", *Cement Concrete Compos.*, **51**, 14-26. https://doi.org/10.1016/j.cemconcomp.2014.03.003.

Ghazy, A., Bassuoni, M.T. and Shalaby, A. (2016), "Nanomodified fly ash concrete: a repair option for concrete pavements", *ACI Mater. J.*, **113**(2), 231-242.

Gjorv, O.E., Monteiro, P.J. and Mehta, P.K. (1990), "Effect of condensed silica fume on the steel-concrete bond", *ACI Mater. J.*, **87**(6), 573-580.

Karagöl, F., Demirbog, R. and Khushefati, W.H. (2015), "Behavior of fresh and hardened concretes with antifreeze admixture in deep-freeze low temperatures and exterior winter conditions", *Constr. Build. Mater.,* **76**, 388–395. https://doi.org/10.1016/j.conbuildmat.2014.12.011.

Kim, J.K., Kim, K.H. and Yang, J.K. (2001), "Thermal analysis of hydration heat in concrete structures with pipe-cooling system", *Comput Struct.*, **79**(2), 163-171. https://doi.org/10.1016/S0045-7949(00)00128-0.

Kim, Y.R., Khil, B.S., Jang, S.J., Choi, W.C. and Yun, H D. (2015), "Effect of barium-based phase change material (PCM) to control the heat of hydration on the mechanical properties of mass concrete", *Thermochim Acta*, **613**, 100-107. https://doi.org/10.1016/j.tca.2015.05.025.

Korhonen, C.L., Cortez, E.R. and Charest, B.A. (1992), "Strength development of concrete cured at low temperature", *Concrete Int.*, **14**(12), 34-39.

LaserComp Inc. (2015), FOX 314 Instrument Manual, Delaware, United States.

Li, X., Chen, H., Li, H., Liu, L., Lu, Z., Zhang, T. and Duan, W.H. (2015), "Integration of form-stable paraffin/nanosilica phase change material composites into vacuum insulation panels for thermal energy storage", *Appl. Energy*, **159**, 601-609. https://doi.org/10.1016/j.apenergy.2015.09.031.

Liu, F., Wang, J. and Qian, X. (2017), "Integrating phase change materials into concrete through microencapsulation using cenospheres", *Cement Concrete Compos.*, **80**, 317-325. https://doi.org/10.1016/j.cemconcomp.2017.04.001.

Lura, P., Plizzari, G.A. and Riva, P. (2002), "3D finite-element modelling of splitting crack propagation", *Mag. Concrete Res*., **54**(6), 481-493. https://doi.org/10.1680/macr.2002.54.6.481.

MacGregor, J.G., Wight, J.K., Teng, S. and Irawan, P. (1997), *Reinforced Concrete: Mechanics and Design*, 3rd Edition, Prentice Hall, Upper Saddle River, New Jersey, United States.

Madani, H., Bagheri, A. and Parhizkar, T. (2012), "The pozzolanic reactivity of monodispersed nanosilica hydrosols and their influence on the hydration characteristics of Portland cement", *Cement Concrete Res*., **42**, 1563-1570. https://doi.org/10.1016/j.cemconres.2012.09.004.

Mahdikhani, M. and Ramezanianpour, A.A. (2014), "Mechanical properties and durability of self consolidating cementitious materials incorporating nano silica and silica fume", *Comput. Concrete*, **14**(2), 175-191. http://dx.doi.org/10.12989/cac.2014.14.2.175.

Memon, S.A., Cui, H., Lo, T.Y. and Li, Q. (2015), "Development of structural–functional integrated concrete with macro-encapsulated PCM for thermal energy storage", *Appl. Energy*, **150**, 245-257. https://doi.org/10.1016/j.apenergy.2015.03.137.

Meshgin, P. and Xi, Y. (2012), "Effect of phase-change materials on properties of concrete", *ACI Mater. J.*, **109**(1), 72-80.

Mills, A.F. (1999), *Basic Heat and Mass Transfer*, Prentice Hall, New Jersey, United States.

Montgomery, D.C. (2017), *Design and Analysis of Experiments*, 9th Edition, Wiley, New Jersey, United States.

Neville, A.M. (2011), *Properties of Concrete*, Prentice Hall, London, UK.

Powers, T.C. and Helmuth, R.A. (1953), "theory of volume changes in hardened portland-cement paste during freezing", *Proceedings of the Thirty-Second Annual Meeting of the Highway Research Board*, Washington, D.C., United Status, January.

Prado, P.J., Balcom, B.J., Beyea, T.W., Armstrong, R.L. and Grattan-Bellew, P.E. (1998), "Concrete freeze/thaw as studied by magnetic resonance Imagine", *Cement Concrete Res.*, **2**(28), 261-270. https://doi.org/10.1016/S0008-8846(97)00222-6.

Ratinov, V.B. and Rozenberg, T.I. (1996), *Antifreezing Admixtures*, Concrete Admixtures Handbook, 2nd Edition, William Andrew Publisher, New York.

RILEM 7-II-128 (1994), RC6: Bond Test for Reinforcing Steel, 1. Pull-out Test for Reinforcement, RILEM (Technical Recommendations for the Testing and Use of Construction Materials, London, UK.

Rixom, M.R. and Mailvaganam, N. (2002), *Chemical Admixture*

for Concrete, CRC Press, Florida, United States.
Ruuska, T., Vinha, J. and Kivioja, H. (2017), "Measuring thermal conductivity and specific heat capacity values of inhomogeneous materials with a heat flow meter apparatus", *J. Build. Eng.*, **9**, 135-141. https://doi.org/10.1016/j.jobe.2016.11.011.
Schroeder, H.P. and Wood, T.B. (1996), "Concrete/reinforcing steel bond strength of low-temperature concrete", *J. Cold. Reg. Eng.*, **10**(2), 93-117. https://doi.org/10.1061/(ASCE)0887-381X(1996)10:2(93).
Tanabe, T.A., Kawasumi, M. and Yamashita, Y. (1985), "Thermal stress analysis of massive concrete", *Finite Element Analysis of Reinforced Concrete Structures*, ASCE, Tokya, Japan, May.
Yankelevsky, D.Z. (1985), "New finite element for bond-slip analysis", *J. Struct. Eng.*, **111**(7), 1533-1542. https://doi.org/10.1061/(ASCE)0733-9445(1985)111:7(1533).
Yankelevsky, D.Z., Jabareen, M. and Abutbul, A.D. (2008), "One-dimensional analysis of tension stiffening in reinforced concrete with discrete cracks", *Eng. Struct.*, **30**(1), 206-217. https://doi.org/10.1016/j.engstruct.2007.03.013.
Yasien, A. and Bassuoni. M. (2019), "Nano-modified concrete at sub-zero temperatures: experimental and statistical modelling", *Mag. Concrete Res.*, **2019**, 1-20. https://doi.org/10.1680/jmacr.19.00437.

SF